Vision Research 86 (2013) 27–34

Contents lists available at SciVerse ScienceDirect

Vision Research

journal homepage: www.elsevier.com/locate/visres

Contribution of the gradient refractive index and shape to the crystalline lens spherical aberration and astigmatism

Judith Birkenfeld *, Alberto de Castro, Sergio Ortiz, Daniel Pascual, Susana Marcos

Instituto de Óptica "Daza de Valdés", Consejo Superior de Investigaciones Científicas, Serrano 121, 28006 Madrid, Spain

ARTICLE INFO

Article history:
Received 27 September 2012
Received in revised form 1 April 2013
Available online 15 April 2013

Keywords:
Crystalline lens
GRIN
Spherical aberration
Astigmatism

ABSTRACT

The optical properties of the crystalline lens are determined by its shape and refractive index distribution. However, to date, those properties have not been measured together in the same lens, and therefore their relative contributions to optical aberrations are not fully understood. The shape, the optical path difference, and the focal length of ten porcine lenses (age around 6 months) were measured *in vitro* using Optical Coherence Tomography and laser ray tracing. The 3D Gradient Refractive Index distribution (GRIN) was reconstructed by means of an optimization method based on genetic algorithms. The optimization method searched for the parameters of a 4-variable GRIN model that best fits the distorted posterior surface of the lens in 18 different meridians. Spherical aberration and astigmatism of the lenses were estimated using computational ray tracing, with the reconstructed GRIN lens and an equivalent homogeneous refractive index. For all lenses the posterior radius of curvature was systematically steeper than the anterior one, and the conic constant of both the anterior and posterior positive surfaces was positive. In average, the measured focal length increased with increasing pupil diameter, consistent with a crystalline lens negative spherical aberration. The refractive index of nucleus and surface was reconstructed to an average value of 1.427 and 1.364, respectively, for 633 nm. The results of the GRIN reconstruction showed a wide distribution of the index in all lens samples. The GRIN shifted spherical aberration towards negative values when compared to a homogeneous index. A negative spherical aberration with GRIN was found in 8 of the 10 lenses. The presence of GRIN also produced a decrease in the total amount of lens astigmatism in most lenses, while the axis of astigmatism was only little influenced by the presence of GRIN. To our knowledge, this study is the first systematic experimental study of the relative contribution of geometry and GRIN to the aberrations in a mammal lens.

1. Introduction

The geometrical and structural properties of the cornea and the crystalline lens as well as their relative alignment determine the aberrations of the optical system of the eye and, therefore, the optical quality of the image projected on the retina. In the young human eye the cornea and crystalline lens partially compensate for each other's aberrations (Barbero et al., 2002; Guirao, Redondo, & Artal, 2000; He et al., 2003a; Sivak & Kreuzer, 1983), particularly spherical aberration and lateral coma (Artal et al., 2001; He et al., 2003b; Kelly, Mihashi, & Howland, 2004; Marcos et al., 2008). In general, the spherical aberration of the young, unaccommodated human lens tends to be negative (Smith et al., 2001) while the cornea usually shows positive spherical aberration (Guirao, Redondo, & Artal, 2000). However, with age the overall spherical aberration of the eye increases towards more positive values (Artal et al., 2002; Barbero, Marcos, & Merayo-Lloves, 2002; Glasser & Campbell, 1998; McLellan, Marcos, & Burns, 2001), likely due to age-related structural changes of the crystalline lens shape and the gradient refractive index.

The compensation effect of cornea and internal optics has been also reported for other low order aberrations such as astigmatism (Read, Collins, & Carney, 2007; Shankar & Bobier, 2004). Other aberrometry-based studies support the trends for corneal/internal balance of spherical aberration (He et al., 2003a; Kelly, Mihashi, & Howland, 2004) and astigmatism (Artal et al., 2001). Kelly et al. suggested that the compensation of spherical aberration was the result of a passive mechanism, while the compensation of astigmatism was individually tuned. Interestingly, the compensation of astigmatism has also been shown to happen at the corneal level with the anterior corneal surface showing higher amounts of astigmatism than the overall (anterior and posterior) cornea (Sicam, Dubbelman, & Van der Heijde, 2006).

Most of the above conclusions on the compensatory mechanisms of cornea and crystalline lens aberrations result from corneal and total aberrometry (or corneal and total refraction), and as a re-

* Corresponding author. Fax: +34 915645557.
E-mail address: j.birkenfeld@csic.es (J. Birkenfeld).

0042-6989/$ - see front matter © 2013 Elsevier Ltd. All rights reserved.
http://dx.doi.org/10.1016/j.visres.2013.04.004

sult, the contribution of the crystalline lens to the effect is estimated indirectly. The contributions of anterior and posterior cornea to the overall aberrations were obtained by direct methods of corneal aberrometry.

Although there is extensive literature that studies theoretically (Blaker, 1980; Smith, Pierscionek, & Atchison, 1991) or experimentally (Borja et al., 2008; Dubbelman & Van der Heijde, 2001; Glasser & Campbell, 1999; Jones et al., 2005; Koretz et al., 1989; Maceo et al., 2011; Moffat, Atchison, & Pope, 2002; Uhlhorn et al., 2008) the contribution of surface shape and index of refraction (generally based on an equivalent homogeneous refractive index) to the lens power, to our knowledge there is no study that measures directly the contribution of lens shape and structure in the overall aberrations of the lens. This work systematically investigates the contribution of the refractive gradient index (GRIN) and the geometry to optical aberration by combining experimental data of lens surface geometry and GRIN profiles on the same specimen.

The gradient refractive index has been measured in several species: fish (Garner et al., 2001; Jagger, 1992; Verma et al., 2007); rat (Campbell, 1984); cat (Jagger, 1990); rabbit (Nakao et al., 1968; Pierscionek, 1993); porcine (de Castro et al., 2010; Pierscionek, Belaidi, & Bruun, 2005; Vazquez et al., 2006), and human (de Castro et al., 2011a; Jones et al., 2005; Kasthurirangan et al., 2008; Pierscionek, 1993, 1997), using both, direct destructive (Nakao et al., 1968; Pierscionek, 1993, 1997) and indirect non-destructive methods using ray tracing (Campbell, 1984; Garner et al., 2001; Pierscionek, Belaidi, & Bruun, 2005; Vazquez et al., 2006); MRI (Garner et al., 2001; Jones et al., 2005; Kasthurirangan et al., 2008), and OCT (de Castro et al., 2010, 2011a; Verma et al., 2007).

To our knowledge, the only systematic experimental analysis of the role of the GRIN on spherical aberration has been performed on fish lenses. Fish lenses are known to have very low amounts of spherical aberration, despite being nearly spherical in shape. Jagger (1992) compared the expected spherical aberration of an artificial spherical lens with homogenous index of refraction with that of the fish lens, and hypothesized that the presence of a GRIN distribution in the lens balanced the lens surface spherical aberration. Kröger et al. (1994) demonstrated the relative contribution (and balance) of the lens surface and GRIN on spherical aberration in African teleost fish lenses. A more recent study used Optical Coherence Tomography in combination with an iterative optical path fitting to estimate the GRIN distribution in zebrafish (Verma et al., 2007). In this study we used a custom-developed spectral OCT system (Grulkowski et al., 2009) to measure in 3D shape and GRIN distribution in porcine lenses.

Extensive work on porcine lenses has been done in recent years, including biometry (Vilupuru & Glasser, 2001), wave aberrations (Roorda & Glasser, 2004), and GRIN estimations (de Castro et al., 2010). Despite various differences with respect to primate lenses (suture line structures, accommodate ability, and geometrical shape), porcine lenses are interesting models to study the relationship between structure, geometry and optical properties, and it seems to be a suitable (Kammel et al., 2012) and common *in vitro* model to test presbyopia correction alternatives such as lens refilling (Koopmans et al., 2004; Wong et al., 2007), or implantation of accommodative intraocular lenses (DeBoer et al., 2012).

In the current study, OCT provided reliable measurements of lens shape in 3D, allowing us to expand previous phakometric measurements of lens shape (limited to lens radius of curvature) to a full characterization including asphericity and astigmatism. Data of optical path difference from OCT and custom developed reconstruction algorithms allowed us to estimate the 3D surface geometry and distribution of the lens GRIN in the same specimen (de Castro et al., 2010). In previous studies (De Castro et al., 2011b), we have demonstrated an accuracy of the GRIN reconstruction with the OCT-based method (for typical errors in the OCT input data) below 5×10^{-3} in terms of GRIN difference root-mean-square, which is comparable to ray tracing-based tomographic techniques (Vazquez et al., 2006). Computational ray tracing gave an estimation of the relative contribution of the lens surface shapes and GRIN to the aberrations of the lens (spherical aberration and astigmatism). To our knowledge, this is the first time that the impact of GRIN on astigmatism and high order aberrations has been studied experimentally in a set of mammal lenses, and sets up basis for further studies in primate lenses.

A broader understanding of the GRIN on spherical aberration is important to gain further insights on the image forming properties of the lens, and, ultimately, to improve the design of intraocular lenses, or other refraction and presbyopic ocular corrections.

2. Material and methods

2.1. Lens specimens and preparation

Ten cadaver porcine eyes (around 6 months of age) were obtained from a local slaughterhouse and transported at a temperature around 4 °C. Experiments were performed within 3–8 h after enucleation.

Immediately before the measurements, the eye globes were cut and the crystalline lens was carefully dissected and placed in a cuvette filled with a preservation solution (DMEM/F-12, HEPES, no phenol red, GIBCO) (Augusteyn et al., 2006). The overall duration of the experiment was about 1 h per lens.

Experimental protocols had been approved by the Institutional Review Boards.

2.2. Optical Coherence Tomography system (OCT)

The lenses were imaged in 3D using a custom developed OCT system. The system is described in detail in a previous publication (Grulkowski et al., 2009), and was provided with fan distortion correction algorithms that arise from the scanning architecture of the instrument (Ortiz et al., 2010). The illumination source was a super luminescent diode (SLD, 840 nm central wavelength, 50 nm (FWHM)). The acquisition speed was 25,000 A-Scans/s. The system is designed for measurements of patients *in vivo*. A 45°-tilted mirror was inserted in the optical path after the collimating beam to allow imaging the lens in a horizontal position (i.e. immersed in solution in a cuvette). The axial resolution predicted by the bandwidth of the SLD laser source is 6.9 μm in tissue. The lens axis was aligned with the OCT scan axis such that a specular reflection was seen from the surfaces of the lens. Care was taken that the lens did not appear tilted in the image preview, for neither 0° nor 90°.

One image contained 1668 A-Scans and 70 B-Scans on a 12×12 mm lateral range. Each set of 3D images consisted of two acquisitions at two different planes of focus which were merged to produce a complete image of anterior surface, posterior surface, and the cuvette holding the lens, using customized MatLab programs (de Castro et al., 2010). The acquisition time for each OCT image was 4.5 s.

2.3. Laser Ray Tracing (LRT)

A custom developed LRT system was used to measure the focal length of the lenses for two different pupil diameters. Illumination came from an 849 nm SLD (Superlum, Cork, Ireland). The beam diameter at the plane of the lens was 600 μm. A 2-mirror galvanometric scanning system, in combination with a 400 mm collimating lens was used to scan rings of light of 2 and 4 mm diameter onto the lens surface. A CMOS camera placed behind the cuvette captured a series of through-focus images around the focal plane

of the system composed by the lens immersed in preservation media and the cuvette. The step size from image to image was set to 0.5 mm. The lens was aligned such that the center of the rays captured with the CMOS camera would not change within the range of movement of the camera (35 mm).

The system was calibrated with commercial artificial lenses (Edmund Optics Inc., Barrington, NJ, USA). Comparison of the back focal length estimates from the experimental system with computational ray tracing programs (Zemax, Radiant Zemax, Redmond, WA, USA) allowed estimation of the back focal length of the lens in preservation media. The precision of the measurements was estimated to be 0.8 mm. The back focal length could be expressed in diopters as the inverse of the back focal length multiplied by the group refractive index of the solution $n = 1.345$ at 825 nm (Borja et al., 2010). The configuration of the system was such that only one focal point was detected, and therefore estimates of potential astigmatism were not available.

To estimate spherical aberration from the experimental power measurements it was assumed that the focal length measured for a circle of light with a radius of $r = 1$ mm corresponds to the paraxial focal length. The 4th order Zernike spherical aberration Z_4^0 was then obtained using

$$Z_4^0 = \frac{Mr^2}{12\sqrt{5}} \quad (1)$$

where M is the difference in power, experimentally determined between the paraxial (2 mm diameter) and the non-paraxial ring (4 mm diameter), and r is the pupil radius, in our measurements 2 mm (Tarrant, Roorda, & Wildsoet, 2010).

2.4. Experimental protocols

All lenses were imaged in the cuvette immersed in preservation medium, first with the OCT system and then with the Laser Ray Tracing (LRT) apparatus.

OCT 3D imaging was performed with the posterior surface lens facing the OCT beam (posterior up image). The lens was then flipped around a predetermined horizontal axis (the same for all lenses) to image it again, this time with the anterior surface facing the OCT beam (anterior up image). The procedure is similar to that described in prior publications (Borja et al., 2010; de Castro et al., 2010).

After completing the OCT imaging, the lens in the cuvette was aligned in the LRT with the anterior surface facing up. A through focus series of 10–15 images was collected with the CMOS camera to estimate the back focal length of the lens.

2.5. OCT image data processing

The OCT images were used to obtain the shape of the anterior and posterior lens surfaces, the thickness of the lens and the optical path accumulated by the rays passing through the lens and arriving to the cuvette, which served (along with the focal length measurements) as input parameters in a GRIN reconstruction algorithm.

The image processing algorithms were described in detail in an earlier publication (de Castro et al., 2010). Custom-developed software was used to merge the images of the lens obtained in two different planes (using the lens holder for registration), and to detect both surfaces of the lens, as well as the cuvette distorted by the lens and preservation medium. The data were corrected from fan distortion (Ortiz et al., 2009). The distortions due to the preservation medium were corrected to extract the geometry of the first surface of each image.

The detected edges of the distorted lens surface – i.e. subject to the optical distortion produced by refraction by the preceding lens surface (Ortiz et al., 2010) and GRIN (Siedlecki et al., 2012), the undistorted surfaces and the cuvette were fitted by Zernike polynomials (up to 7th order) within a 6 mm pupil. However, since the ray tracing algorithm is defined assuming conic surfaces, only symmetric Zernike polynomials and astigmatism were used to implement the lens surfaces in the algorithm. The radii of curvature and conic constants (Manns et al., 2004) were calculated for 18 meridians. Previous studies using the same instrument estimate an accuracy in radius of curvature of 1% in glass lenses (Ortiz et al., 2010), and test–retest variability *in vivo* of similar amount (Ortiz et al., 2011). Some of the variability is associated to interdependences between radius of curvature and conic constant in a conic fitting (Pérez-Escudero et al., 2010). Maximum and minimum radii of curvature and conic constants across meridians are reported. The lens thickness was calculated using the method proposed by Uhlhorn et al. (2008).

2.6. GRIN reconstruction algorithm

An updated version of the GRIN reconstruction algorithm proposed by de Castro et al. (2010) was used to estimate the 3D GRIN distribution within the central 6 mm pupil diameter of the lens. Input parameters were lens shape and thickness, as well as the optical path obtained from the OCT images. A novelty of the new algorithm is the use of focal length data (for 2-mm and 4-mm ring diameters) as additional input parameters. The GRIN was reconstructed searching for the parameters of the refractive index distribution which best fits the experimental data. The procedure was applied in 18 lens meridians, from 0 to 170 in steps of 10°.

The algorithm was run five times for each data set. The group refractive index at 849 nm was reconstructed (since the OCT system uses a broadband source) and was then converted to phase refractive index at 633 nm (Uhlhorn et al., 2008) for comparison with previous publications. The main features of the reconstruction algorithm are explained in detail in a previous publication (de Castro et al., 2010), and are only reviewed in brief below.

2.6.1. GRIN model

The GRIN is described as a 4-variable model (see Fig. 1), in which the refractive index varies from the nucleus to the surface in both the axial and meridional directions, and is expressed in polar coordinates as

$$n(\rho,\theta) = n_N - \Delta n \cdot \left(\frac{\rho}{\rho_s}\right)^{p(\theta)} \quad (2)$$

where n_N is the refractive index of the nucleus, Δn is the difference between surface and nucleus, ρ_s is the distance between nucleus and surface, and $p(\theta)$ is the exponential decay that can be different in axial ($p1$) and meridional ($p2$) direction. $p1$ was constrained to

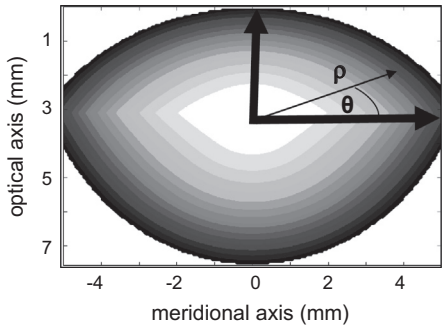

Fig. 1. The GRIN was described in each meridian by four variables; nucleus and surface refractive index, and exponential decay in optical and meridional axis. The center of the lens was set to 0.41 times the central thickness of the lens, and the refractive index in each point was calculated in polar coordinates with Eq. (2).

have the same value in all meridians while $p2$ could vary to account for differences between meridians. The center of the GRIN was defined to be in the optical axis at a distance from the anterior surface vertex equal to 0.41 times the lens thickness (Rosen et al., 2006).

2.6.2. Search algorithm

The global search algorithm is based on a genetic optimization algorithm (Holland, 1975), which avoids the solution falling in local minima. The GRIN parameters that best fit the experimental values are searched by minimizing a Merit function. The Merit function is defined by the sum of the RMS (root mean square) of the differences between simulated and measured OPD (optical path difference) for the posterior surface of the crystalline lens and the cuvette (de Castro et al., 2010), and the difference between the simulated and measured back focal length for the two rings of light projected onto the lens.

2.7. Computational ray tracing analysis

To investigate the relative effect of the lens geometry and GRIN distribution on the aberrations of the lens, a computational ray tracing analysis was performed at multiple meridians, based on the experimental lens parameters retrieved for each meridian of the lens. The custom developed ray tracing algorithm was programmed in MatLab (MathWorks, Natick, MA). The basic components of the algorithm are the implementation of the Stavroudis formula to trace rays through conical surfaces (Stavroudis, 1972), the Sharma algorithm for ray tracing in the GRIN media (Sharma, Kumar, & Ghatak, 1982), and a procedure to calculate the impact of the ray in the posterior surface of the lens (Stone & Forbes, 1990).

Aberrations were calculated for a 6 mm pupil diameter by fitting the wave front up to a 7th order Zernike polynomial expansion using the reconstructed 3D GRIN distribution or the equivalent refractive index. The equivalent refractive index, defined as the homogeneous index of a lens with the same external geometry and focal length as the crystalline lens, was calculated. Astigmatism and spherical aberration coefficient (obtained from the wavefront fitting) were compared across lenses, assuming a homogeneous equivalent refractive index or the estimated GRIN. The astigmatism was calculated with the Zernike polynomials using the power vector defined by Thibos, Wheeler, and Horner (1997).

3. Results

3.1. Lens geometry

All the meridians of the lens surfaces were well fitted with conic sections. The residuals were below 50 μm over the entire central 6 mm pupil.

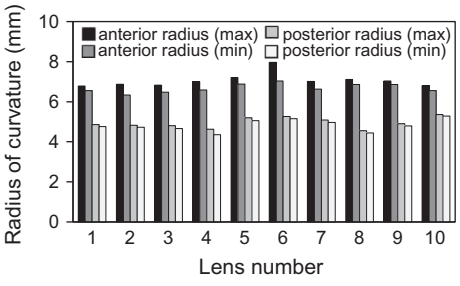

Fig. 2. Radius of curvature of the 10 studied porcine lenses. Data are maximum and minimum radii of curvature from fits to 18 meridians.

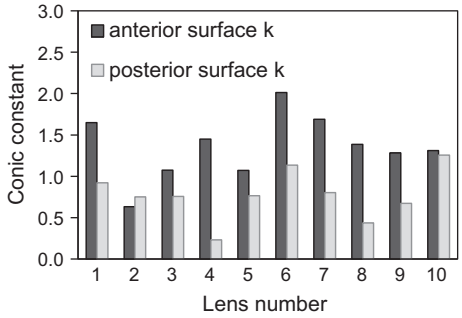

Fig. 3. Asphericity of the 10 studied porcine lenses. Shown is the conic constant $k = Q + 1$ for all lenses. In all cases k was positive for both the anterior and posterior lens surface.

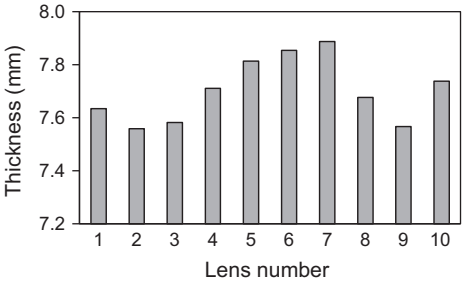

Fig. 4. Calculated lens thickness for all lens samples.

Fig. 2 shows the measured radii of curvature of the anterior and posterior lens surfaces (from anterior and posterior up lens OCT images, respectively) for all lenses. The posterior lens surface is systematically steeper than the anterior surface. A statistically significant correlation between anterior and posterior radius of curvature, reported in previous studies (Vilupuru & Glasser, 2001) was not found.

The astigmatism of anterior and posterior lens surfaces was not aligned, i.e. the axis of astigmatism of posterior surface was rotated with respect to the axis of astigmatism of the anterior surface. The amount of astigmatic axis rotation differed across lenses: in five out of ten lenses the rotation was around 45°, and in two of them nearly 90°. This crossed astigmatism between anterior and posterior lens surfaces is consistent with previous observations *in vitro* (de Castro et al., 2010; porcine lenses) and *in vivo* (Ortiz et al., 2012; human lenses).

Fig. 3 shows the anterior and posterior lens asphericity (conic constant $k = Q + 1$) for all lenses (average across meridians). The values were in the positive range without exception describing the lenses surfaces as prolate ellipsoids ($0 < k < 1$) or oblate ellipsoids ($k > 1$) (Dubbelman, van der Heijde, & Weeber, 2005).

Fig. 4 shows the estimated central thickness of the lenses. Lens thickness ranged from 7.56 mm to 7.89 mm.

3.2. Laser ray tracing

The back focal length of the lenses was studied using a laser ray tracing system which projects circles of lights of different diameters on the lens. The measured back focal length in the preservation medium was on average 21.7 ± 0.8 mm (ranging from 20.4 to 22.7 mm) and 22.0 ± 0.8 mm (ranging from 20.8 to 22.9 mm) for the 2 mm and 4 mm diameter rings of light, respectively, corresponding to a power of 61.9 ± 2.4 D and 61.0 ± 2.1 D in solution, respectively. In nine out of ten lenses a shorter back focal length for a smaller diameter was found. The shorter back focal length

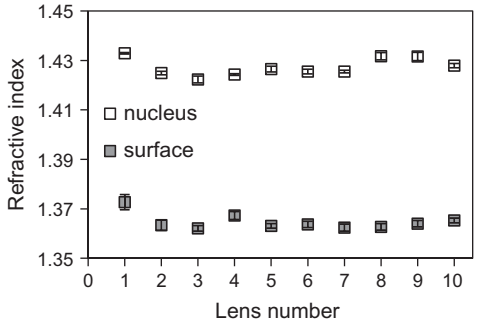

Fig. 5. Nucleus and surface refractive index for the 10 porcine lenses in the study. The standard deviation across repeated reconstruction is indicated for each individual lens. Averaged across lenses the standard deviation was 0.0019 for the nucleus and 0.0030 for the lens surface.

for a smaller diameter is consistent with a negative spherical aberration in the crystalline lenses. Using Eq. (1), the fourth order spherical aberration Z_4^0 was calculated to a mean value of $Z_4^0 = -0.137$ μm.

3.3. Gradient index distribution

3.3.1. Refractive index of nucleus and surface

The reconstructed refractive indices of the lens nucleus and surface are shown in Fig. 5 for all eyes (at a phase refractive index at 633 nm). On average, the refractive index varied from 1.427 in the nucleus to 1.364 in the periphery (the corresponding values at 849 nm are 1.436 and 1.374 for nucleus and periphery, respectively). The standard deviations across repeated reconstructions (averaged across lenses) were 0.0019 for the nucleus, and 0.0030 for the periphery. The standard deviations of the refractive indices across lenses were 0.004 and 0.003 for nucleus and surface, respectively, indicating low differences in the refractive index values across lenses.

Fig. 6 shows examples of the index profile for 2 example lenses. The decay along the optical axes is shown for the anterior and posterior part of the lens. Also shown is the distribution of the decay along multiple meridians (solid line). The meridional variations of the index relate to the meridional GRIN profile differences.

The inset shows the corresponding refractive index distribution for one meridian. Across all lenses, the exponential decay of the GRIN in the optical axis ($p1$ in Eq. (2)) varied from 1.42 to 1.98, and the meridional decay change ($p2$ in Eq. (2)) from 1.64 to 5.52 with a change of 1.3 as a mean between meridians. The low value of the exponential decays means that there is no plateau built up

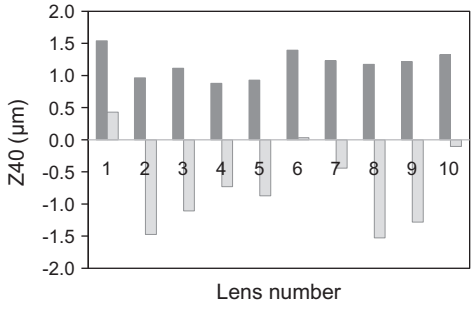

Fig. 7. Fourth order spherical aberrations calculated with the reconstructed GRIN (light gray bars) and the homogeneous equivalent refractive index (dark gray bars). The presence of GRIN shifts the spherical aberration towards negative values. The shift induced by the GRIN varies between 1.12 μm and 2.7 μm.

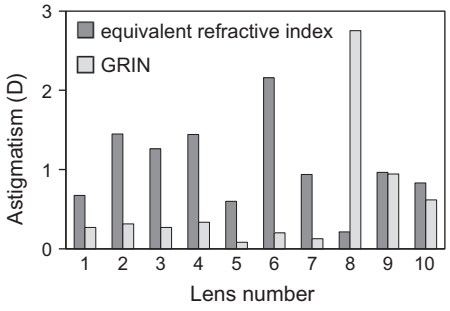

Fig. 8. Amount of astigmatism for lenses with a homogeneous equivalent refractive index and the corresponding GRIN. In most cases the absence of a GRIN implied a higher amount of astigmatism.

along the axis, this is, that the gradient refractive index is well distributed across all lenses.

3.3.2. Equivalent refractive index

The mean equivalent refractive index found across lenses was 1.449 ± 0.003. The standard deviation of the results of the five repetitions of the search algorithm was below the standard deviation across all lenses.

3.3.3. Spherical aberration

Fig. 7 shows the 4th order spherical aberration for all lenses (6 mm pupil diameter), calculated from the measured lens shape and both the reconstructed GRIN distribution and the equivalent refractive index. Results are shown for both the corresponding equivalent refractive index and the measured GRIN distribution.

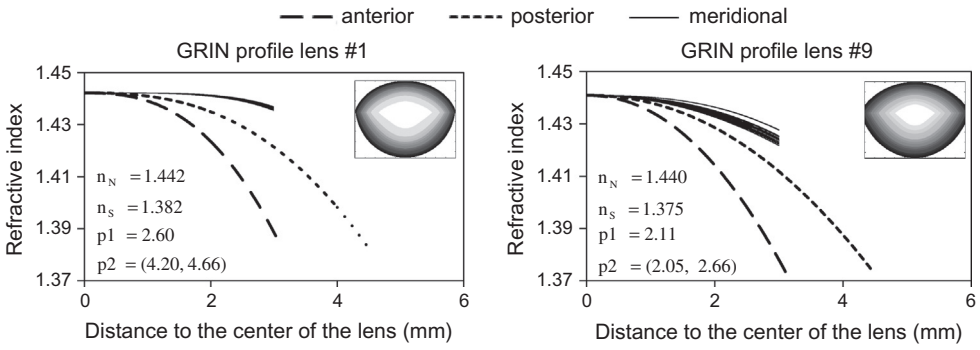

Fig. 6. Refractive index profile from nucleus to surface along the optical axis in the anterior (long dashed line) and posterior (short dashed line) part of the lens and along the meridional direction (continuous line). Insets show the corresponding reconstructed values of nucleus and surface refractive indices (n_N and n_s) and the exponential decay factor $p1$ and $p2$ from Eq. (2). On the upper right side, the GRIN distribution map is shown for a single meridian.

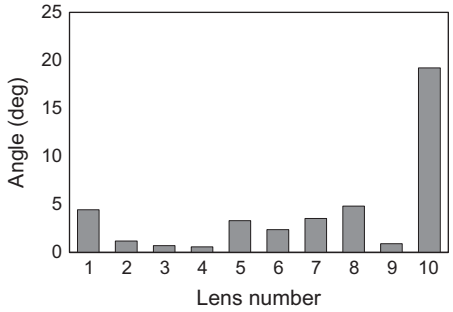

Fig. 9. Change of astigmatic angle induced by the GRIN. The values are less than 5° in almost all cases.

Spherical aberration was consistently positive with the homogeneous index (1.17 ± 0.21 μm) and shifted towards negative values in the presence of GRIN (−0.71 ± 0.67 μm). GRIN shifted spherical aberration between 1.12 μm and 2.7 μm. A negative spherical aberration was found in 8 out of the 10 lenses.

3.3.4. Astigmatism

Fig. 8 shows the amount of astigmatism in the lens for an equivalent refractive index lens and the corresponding GRIN lens. Sources of astigmatism in the lens are the astigmatism of each of the surfaces as well as the meridional variations in the GRIN. In most lenses the presence of GRIN produced a decrease in the total amount of astigmatism in the lens. Only in one lens (#8) astigmatism increased with GRIN, whereas in two lenses (#9 and #10) GRIN seems to play a minor role in lens astigmatism.

Fig. 9 shows the estimated axis of astigmatism with a homogenous index and GRIN. The presence of GRIN induces very little rotation in the angle of astigmatism (4.11° on average). Except for lens #10, the rotation induced by the GRIN was less than 5°.

4. Discussion

We characterized the geometry, GRIN and optical aberrations of several young porcine crystalline lenses *in vitro*. To our knowledge, this is the first systematic experimental study of the relative contribution of geometry and GRIN to the aberrations in a mammal lens, and the first time that the study of the crystalline lens geometry and GRIN has been addressed in three dimensions.

Experimental measurements of GRIN in mammals are scarce. (Vazquez et al., 2006) reported 2D GRIN profiles in porcine lenses, using a tomographic reconstruction technique based on lateral ray tracing. Their reported index values ranged from 1.366 to 1.444 (mono-polynomial model) and 1.361 and 1.449 (by-polynomial model) for the surface and the nucleus refractive index, respectively. In a previous publication, de Castro et al. (2010) found 1.362 and 1.443 with a similar reconstruction method to that presented in the current study, but based on OCT images only. Those data are in close agreement with our findings (1.364 and 1.427 for surface and nucleus indices) using both OCT and focal length as input measurements.

Vilupuru et al. studied the biometrical and optical properties of the isolated pig lenses using a scanner laser apparatus (Vilupuru & Glasser, 2001). The lens radii of curvature values in our current study (6.5–7.5 mm for the anterior lens and 4.5–5.3 mm for the posterior lens) fall within the ranges reported by Vilupuru et al. (5.5–7.5 mm and 5–7 mm, respectively). Unlike in their study, no significant correlations between the dimensions of the anterior and posterior lens were found, most likely because of the limited age range of the subjects in this study and, therefore, more similar lens geometry across the sample (all eyes were around 6 months of age in our study, compared to 3–8 years in the previous study).

To our knowledge, asphericities in the porcine lens have never been reported. Interestingly, unlike the primate lens, which tends to show negative asphericity in the lens surfaces *in vivo* and *in vitro* (Borja et al., 2008; Dubbelman & Van der Heijde, 2001), we found positive and negative asphericities in the anterior and posterior surfaces. And unlike the great intersubject variability in lens asphericities found *in vivo* (Dubbelman & Van der Heijde, 2001), we found relatively low intersubject variability in the asphericity measured in this group of pigs.

The focal length measured in this study (ranging from 20.4 to 22.7 mm and from 20.8 to 22.9 mm respectively for the 2 mm and 4 mm diameter rings of light, respectively), seemed in general lower than the ones by Vilupuru et al. with laser scan measurements who reported a wide range of values (around 23–34 mm) (Vilupuru & Glasser, 2001). Contrarily, a study by Jones and Pope (2004) measured the focal length of six different porcine lenses (age unknown) with both optical methods and MRI measurements, and reported in average a shorter focal length (19.0 ± 1.2 mm for ray tracing and 19.6 ± 0.77 using the GRIN estimated with MRI) than the one in the present study. The differences may arise from the mentioned differences in age.

The results from the ray tracing measurements showed negative spherical aberration in most of the lenses. As expected, since these data were used as input values in the GRIN reconstruction, the ray tracing estimates of spherical aberration based on the lens shape and GRIN are consistent with those negative values. The calculated spherical aberration using the reconstructed GRIN was −0.71 μm (for a 6 mm pupil diameter). The lower value found from laser ray tracing (−0.137 μm) is consistent with the smaller sampled lens area in the experimental measurements (4 mm diameter).

The spherical aberration calculated using the reconstructed GRIN is similar to the spherical aberration reported using laser ray tracing (Roorda & Glasser, 2004) on a single porcine lens (around −1 μm for a 6-mm pupil diameter) and the results using a point-diffraction interferometer (Acosta et al., 2010) on 12 porcine lenses (around −1 μm for a 6 mm pupil diameter). Also, most porcine lenses (16 out of 20) studied by Vilupuru et al. showed negative spherical aberration but the data showed a high variability (Vilupuru & Glasser, 2001). The reported mean spherical was equivalent to a much higher Zernike spherical aberration value (−2.5 ± 3.4 μm) than our results. An earlier study, in which beams from a He Ne laser of varying separations were directed through crystalline lenses of a number of vertebrates, found pig lenses to be almost free of aberration (Sivak & Kreuzer, 1983).

The results of the optimization show low exponential decay values in all the lenses, which means a smooth variation of the index of refraction within the porcine lenses studied. This is more similar to the young human lens, whose refractive index varies smoothly from surface to nucleus and can be approximated with a model with low exponential decay value, than to the aging human lens, which shows a rapid change of refractive index near the surface and a plateau of constant refractive index in the center of the lens and, therefore, can be approximated with a model with high exponential decay values (de Castro et al., 2011a; Jones et al., 2005).

Our results show that the GRIN distribution plays an important role in the negative spherical aberration of the crystalline lens in pig. The shift of spherical aberration towards negative values with the GRIN in pig lenses had been suggested by Vazquez (2007) and was also apparent in the experimental study by Wong et al. (2007) on polymer refilled pig lenses. Wong et al. reported that the spherical aberration of a lens refilled with a homogeneous refractive index gel was positive, while it was negative before refilling. This compensation of the surface positive spherical aberration by the

GRIN is well known in spherical and nearly spherical lenses such as in fish (Jagger, 1992; Kröger et al., 1994) where the lens spherical aberration is close to zero. In fish, potential corneal aberrations are irrelevant due to the water immersion. In humans, the negative spherical aberration of the crystalline lens serves to compensate the positive spherical aberration of the cornea (Artal et al., 2002; Barbero, Marcos, & Merayo-Lloves, 2002). This was also reported in primates (Roorda & Glasser, 2004), and may be also the case in pigs.

Similarly to spherical aberration, compensatory effects of corneal astigmatism by lenticular astigmatism have been previously reported (Artal et al., 2002; Kelly, Mihashi, & Howland, 2004). Population studies conclude that the crystalline lens compensates about 0.5 D of corneal astigmatism in human eyes (Read, Collins, & Carney, 2007). As for spherical aberration, the balance of astigmatism tends to be lost with age, by a prevalent shift of corneal astigmatism from with-the rule to against the rule with age (Saunders, 1984). While the internal astigmatism is generally evaluated indirectly from corneal keratometry or corneal topography and ocular refractions, the sources of lenticular astigmatism have generally not been investigated. By measuring the lens shapes and GRIN we have been able to analyze the contribution of the astigmatism of the anterior and posterior lens surfaces and the GRIN distribution to the astigmatism of the porcine lens. Interestingly, the magnitude of the astigmatism was lower in the lens with the reconstructed GRIN than in the lens with the homogeneous index in 8 out of 10 lenses, although the presence of GRIN generally did not entailed a relevant change in astigmatism axis.

In summary, we have investigated the contribution of the gradient refractive index and shape to the crystalline lens spherical aberration and astigmatism for the first time in a mammal lens. Understanding the sources of these aberrations in the human lens is particularly important in the development of intraocular lenses. Aspheric and toric designs aim at mimicking the compensatory role of the corneal aberrations by the young lens. Better designs can be envisioned by a gaining deeper knowledge of the strategies followed in natural lenses, including different animal species.

Acknowledgments

We acknowledge financial support from Grant FIS2011-25637 (Spanish Government) and ERC 2011 Advanced Grant 294099 (European Research Council) to S.M., CSIC JAE Program Fellowship to J.B. We acknowledge technical support from Enrique Gambra and Pablo Pérez-Merino (Visual Optics and Biophotonics Lab) and Andrés Ferrer (Instituto de Óptica) in the early stages of the work.

References

Acosta, E., Bueno, J. M., Schwarz, C., & Artal, P. (2010). Relationship between wave aberrations and histological features in ex vivo porcine crystalline lenses. *Journal of Biomedical Optics, 15*(5), 055001.

Artal, P., Guirao, A., Berrio, E., & Williams, D. R. (2001). Compensation of corneal aberrations by the internal optics in the human eye. *Journal of Vision, 1*(1), 1–8. http://dx.doi.org/10:1167/1.1.1.

Artal, P., Berrio, E., Guirao, A., & Piers, P. (2002). Contribution of the cornea and internal surfaces to the change of ocular aberrations with age. *Journal of the Optical Society of America A, 19*(1), 137–143.

Augusteyn, R. C., Rosen, A. M., Borja, D., Ziebarth, N. M., & Parel, J. M. (2006). Biometry of primate lenses during immersion in preservation media. *Molecular Vision, 12*, 740–747.

Barbero, S., Marcos, S., & Merayo-Lloves, J. (2002). Corneal and total optical aberrations in a unilateral aphakic patient. *Journal of Cataract and Refractive Surgery, 28*(9), 1594–1600.

Barbero, S., Marcos, S., Merayo-Lloves, J., & Moreno-Barriuso, E. (2002). Validation of the estimation of corneal aberrations from videokeratography in keratoconus. *Journal of Refractive Surgery, 18*(3), 263–270.

Blaker, J. W. (1980). Toward an adaptive model of the human eye. *Journal of the Optical Society of America, 70*(2), 220–223.

Borja, D., Manns, F., Ho, A., Ziebarth, N., Rosen, A. M., Jain, R., et al. (2008). Optical power of the isolated human crystalline lens. *Investigative Ophthalmology and Visual Science, 49*(6), 2541–2548.

Borja, D., Siedlecki, D., de Castro, A., Uhlhorn, S., Ortiz, S., Arrieta, E., et al. (2010). Distortions of the posterior surface in optical coherence tomography images of the isolated crystalline lens: Effect of the lens index gradient. *Biomedical Optics Express, 1*(5), 1331–1340.

Campbell, M. C. (1984). Measurement of refractive index in an intact crystalline lens. *Vision Research, 24*(5), 409–415.

de Castro, A., Ortiz, S., Gambra, E., Siedlecki, D., & Marcos, S. (2010). Three-dimensional reconstruction of the crystalline lens gradient index distribution from OCT imaging. *Optics Express, 18*(21), 21905–21917.

de Castro, A., Siedlecki, D., Borja, D., Uhlhorn, S., Parel, J. M., Manns, F., et al. (2011a). Age-dependent variation of the gradient index profile in human crystalline lenses. *Journal of Modern Optics, 58*(19–20), 1781–1787.

DeBoer, C., Do, Hyung Wan, Lee, J., Humayun, M., & Tai, Yu-Chong (2012). Biomimetic accommodating intraocular lens (IOL). In *IEEE 25th international conference on micro electro mechanical systems (MEMS)* (pp. 926–929).

Dubbelman, M., & Van der Heijde, G. (2001). The shape of the aging human lens: Curvature, equivalent refractive index and the lens paradox. *Vision Research, 41*(14), 1867–1877.

Dubbelman, M., van der Heijde, R. G. L., & Weeber, H. A. (2005). Change in shape of the aging human crystalline lens with accommodation. *Vision Research, 45*(1), 117–132.

Garner, L. F., Smith, G., Yao, S., & Augusteyn, R. C. (2001). Gradient refractive index of the crystalline lens of the Black Oreo Dory (Allocyttus Niger): Comparison of magnetic resonance imaging (MRI) and laser ray tracing methods. *Vision Research, 41*(8), 973–979.

Glasser, A., & Campbell, M. C. W. (1998). Presbyopia and the optical changes in the human crystalline lens with age. *Vision Research, 38*(2), 209–229.

Glasser, A., & Campbell, M. C. W. (1999). Biometric, optical and physical changes in the isolated human crystalline lens with age in relation to presbyopia. *Vision Research, 39*(11), 1991–2015.

Grulkowski, I., Gora, M., Szkulmowski, M., Gorczynska, I., Szlag, D., Marcos, S., et al. (2009). Anterior segment imaging with Spectral OCT system using a high-speed CMOS camera. *Optics Express, 17*(6), 4842–4858.

Guirao, A., Redondo, M., & Artal, P. (2000). Optical aberrations of the human cornea as a function of age. *Journal of the Optical Society of America A, 17*(10), 1697–1702.

He, J. C., Gwiazda, J., Thorn, F., & Held, R. (2003a). Wave-front aberrations in the anterior corneal surface and the whole eye. *Journal of the Optical Society of America A, 20*(7), 1155–1163.

He, J. C., Gwiazda, J., Thorn, F., Held, R., & Huang, W. (2003b). Change in corneal shape and corneal wave-front aberrations with accommodation. *Journal of Vision, 3*(7). http://dx.doi.org/10.1167/3.7.1.

Holland, J. (1975). *Adaptation in natural and artificial systems*. University of Michigan Press.

Jagger, W. S. (1990). The refractive structure and optical properties of the isolated crystalline lens of the cat. *Vision Research, 30*(5), 723–738.

Jagger, W. (1992). The optics of the spherical fish lens. *Vision Research, 32*(7), 1271–1284.

Jones, C., & Pope, J. (2004). Measuring optical properties of an eye lens using magnetic resonance imaging. *Magnetic Resonance Imaging, 22*(2), 211–220.

Jones, C. E., Atchison, D. A., Meder, R., & Pope, J. M. (2005). Refractive index distribution and optical properties of the isolated human lens measured using magnetic resonance imaging (MRI). *Vision Research, 45*(18), 2352–2366.

Kammel, R., Ackermann, R., Mai, T., Damm, C., & Nolte, S. (2012). Pig lenses in a lens stretcher: Implications for presbyopia treatment. *Optometry and Vision Science, 89*(6), 908–915.

Kasthurirangan, S., Markwell, E. L., Atchison, D. A., & Pope, J. M. (2008). In vivo study of changes in refractive index distribution in the human crystalline lens with age and accommodation. *Investigative Ophthalmology and Visual Science, 49*(6), 2531–2540.

Kelly, J. E., Mihashi, T., & Howland, H. C. (2004). Compensation of corneal horizontal/vertical astigmatism, lateral coma, and spherical aberration by internal optics of the eye. *Journal of Vision, 4*(4). http://dx.doi.org/10.1167/4.4.2.

Koopmans, S. A., Terwee, T., Haijtema, H. J., Deuring, H., Aarle, S., & Kooijman, A. C. (2004). Relation between injected volume and optical parameters in refilled isolated porcine lenses. *Ophthalmic and Physiological Optics, 24*(6), 572–579.

Koretz, J. F., Kaufman, P. L., Neider, M. W., & Goeckner, P. A. (1989). Accommodation and presbyopia in the human eye – Aging of the anterior segment. *Vision Research, 29*(12), 1685–1692.

Kröger, R. H., Campbell, M. C., Munger, R., & Fernald, R. D. (1994). Refractive index distribution and spherical aberration in the crystalline lens of the African cichlid fish *Haplochromis burtoni*. *Vision Research, 34*(14), 1815–1822.

Maceo, B. M., Manns, F., Borja, D., Nankivil, D., Uhlhorn, S., Arrieta, E., et al. (2011). Contribution of the crystalline lens gradient refractive index to the accommodation amplitude in non-human primates: In vitro studies. *Journal of Vision, 11*(13). http://dx.doi.org/10.1167/11.13.23.

Marcos, S., Rosales, P., Llorente, L., Barbero, S., & Jiménez-Alfaro, I. (2008). Balance of corneal horizontal coma by internal optics in eyes with intraocular artificial lenses: Evidence of a passive mechanism. *Vision Research, 48*(1), 70–79.

McLellan, J. S., Marcos, S., & Burns, S. A. (2001). Age-related changes in monochromatic wave aberrations of the human eye. *Investigative Ophthalmology and Visual Science, 42*(6), 1390–1395.

Moffat, B. A., Atchison, D. A., & Pope, J. M. (2002). Age-related changes in refractive index distribution and power of the human lens as measured by magnetic resonance micro-imaging in vitro. *Vision Research, 42*(13), 1683–1693.

Nakao, S., Fujimoto, S., Nagata, R., & Iwata, K. (1968). Model of refractive-index distribution in the rabbit crystalline lens. *Journal of the Optical Society of America, 58*(8), 1125–1130.

Ortiz, S., Siedlecki, D., Remon, L., & Marcos, S. (2009). Optical coherence tomography for quantitative surface topography. *Applied Optics, 48*(35), 6708–6715.

Ortiz, S., Siedlecki, D., Grulkowski, I., Remon, L., Pascual, D., Wojtkowski, M., et al. (2010). Optical distortion correction in optical coherence tomography for quantitative ocular anterior segment by three-dimensional imaging. *Optics Express, 18*(3), 2782–2796.

Ortiz, S., Pérez-Merino, P., Gambra, E., de Castro, A., & Marcos, S. (2012). In vivo human crystalline lens topography. *Biomedical Optics Express, 10*(3), 2471–2488.

Pierscionek, B. K. (1993). Surface refractive index of the eye lens determined with an optic fiber sensor. *Journal of the Optical Society of America, 10*(9), 1867–1871.

Pierscionek, B. K. (1997). Refractive index contours in the human lens. *Experimental Eye Research, 64*(6), 887–893.

Pierscionek, B. K., Belaidi, A., & Bruun, H. H. (2005). Refractive index distribution in the porcine eye lens for 532 nm and 633 nm light. *Eye (London), 19*(4), 375–381.

Read, S. A., Collins, M. J., & Carney, L. G. (2007). A review of astigmatism and its possible genesis. *Clinical and Experimental Optometry, 90*(1), 5–19.

Roorda, A., & Glasser, A. (2004). Wave aberrations of the isolated crystalline lens. *Journal of Vision, 4*(4), 250–261.

Rosen, A. M., Denham, D. B., Fernandez, V., Borja, D., Ho, A., Manns, F., et al. (2006). In vitro dimensions and curvatures of human lenses. *Vision Research, 46*(6–7), 1002–1009.

Saunders, H. (1984). The astigmatic modulus and its age-dependence. *Ophthalmic and Physiological Optics, 4*(3), 215–222.

Shankar, S., & Bobier, W. R. (2004). Corneal and lenticular components of total astigmatism in a preschool sample. *Optometry and Vision Science, 81*(7), 536–542.

Sharma, A., Kumar, D. V., & Ghatak, A. K. (1982). Tracing rays through graded-index media: A new method. *Applied Optics, 21*(6), 984–987.

Sicam, V. A. D. P., Dubbelman, M., & Van der Heijde, R. G. L. (2006). Spherical aberration of the anterior and posterior surfaces of the human cornea. *Journal of the Optical Society of America A, 23*(3), 544–549.

Sivak, J., & Kreuzer, R. (1983). Spherical aberration of the crystalline lens. *Vision Research, 23*(1), 59–70.

Smith, G., Cox, M. J., Calver, R., & Garner, L. F. (2001). The spherical aberration of the crystalline lens of the human eye. *Vision Research, 41*(2), 235–243.

Smith, G., Pierscionek, B. K., & Atchison, D. A. (1991). The optical modelling of the human lens. *Ophthalmic and Physiological Optics, 11*(4), 359–369.

Stavroudis, O. N. (1972). *The optics of rays, wavefronts, and caustics*. Academic Press Inc.

Stone, B. D., & Forbes, G. (1990). Optimal interpolants for Runge-Kutta ray tracing in inhomogeneous media. *Journal of the Optical Society of America A, 7*(2), 248–254.

Thibos, L. N., Wheeler, W., & Horner, D. (1997). Power vectors: An application of Fourier analysis to the description and statistical analysis of refractive error. *Optometry and Vision Science, 74*(6), 367.

Uhlhorn, S. R., Borja, D., Manns, F., & Parel, J. M. (2008). Refractive index measurement of the isolated crystalline lens using optical coherence tomography. *Vision Research, 48*(27), 2732–2738.

Vazquez, D. (2007). Tomographic reconstruction of the gradient indices with rotational symmetry. Application to crystalline lenses. PhD thesis. Universidad de Santiago de Compostela.

Vazquez, D., Acosta, E., Smith, G., & Garner, L. (2006). Tomographic method for measurement of the gradient refractive index of the crystalline lens. II. The rotationally symmetrical lens. *Journal of the Optical Society of America A, 23*(10), 2551–2565.

Verma, Y., Rao, K., Suresh, M., Patel, H., & Gupta, P. (2007). Measurement of gradient refractive index profile of crystalline lens of fisheye in vivo using optical coherence tomography. *Applied Physics B, 87*(4), 607–610.

Vilupuru, A. S., & Glasser, A. (2001). Optical and biometric relationships of the isolated pig crystalline lens. *Ophthalmic and Physiological Optics, 21*(4), 296–311.

Wong, K. H., Koopmans, S. A., Terwee, T., & Kooijman, A. C. (2007). Changes in spherical aberration after lens refilling with a silicone oil. *Investigative Ophthalmology and Visual Science, 48*(3), 1261–1267.